

See discussions, stats, and author profiles for this publication at: <https://www.researchgate.net/publication/263946462>

# Insights into Adsorption of NH<sub>3</sub> on HKUST-1 Metal–Organic Framework: A Multitechnique Approach

ARTICLE in THE JOURNAL OF PHYSICAL CHEMISTRY C · SEPTEMBER 2012

Impact Factor: 4.77 · DOI: 10.1021/jp305756k

---

CITATIONS

34

READS

29

## 7 AUTHORS, INCLUDING:



Sara Maurelli

Università degli Studi di Torino

23 PUBLICATIONS 181 CITATIONS

[SEE PROFILE](#)



Diego Gianolio

Diamond Light Source

47 PUBLICATIONS 553 CITATIONS

[SEE PROFILE](#)



Mario Chiesa

Università degli Studi di Torino

99 PUBLICATIONS 1,724 CITATIONS

[SEE PROFILE](#)



Carlo Lamberti

Università degli Studi di Torino

378 PUBLICATIONS 12,760 CITATIONS

[SEE PROFILE](#)

# Insights into Adsorption of NH<sub>3</sub> on HKUST-1 Metal–Organic Framework: A Multitechnique Approach

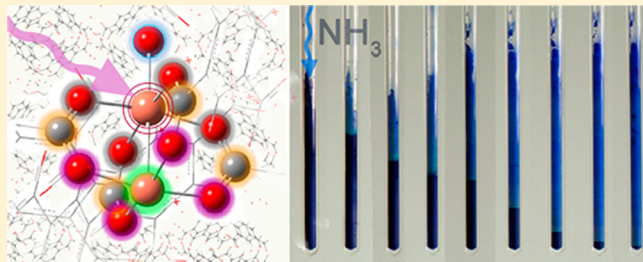
Elisa Borfecchia,<sup>†</sup> Sara Maurelli,<sup>†</sup> Diego Gianolio,<sup>‡</sup> Elena Groppo,<sup>†</sup> Mario Chiesa,<sup>†</sup> Francesca Bonino,<sup>\*,†</sup> and Carlo Lamberti<sup>†</sup>

<sup>†</sup>Department of Chemistry, NIS Centre of Excellence, and INSTM Reference Center, University of Turin, Via P. Giuria 7, I-10125 and Via Quarello 11, I-10135, Torino, Italy

<sup>‡</sup>Diamond Light Source Ltd., Harwell Science and Innovation Campus, Didcot OX11 0DE, United Kingdom

## Supporting Information

**ABSTRACT:** We report a careful characterization of the interaction of NH<sub>3</sub> with the Cu(II) sites of the [Cu<sub>2</sub>C<sub>4</sub>O<sub>8</sub>] paddle-wheel cornerstone of the HKUST-1 metallorganic framework, also known as Cu<sub>3</sub>(BTC)<sub>2</sub>. The general picture emerging from combining XRPD, EXAFS, XANES, mid- and far-IR, DRUV-vis, and EPR techniques is that the presence of traces of water has relevant consequences on the effect of ammonia on the MOF framework. NH<sub>3</sub> adsorption on the dry system results in a strong chemisorption on Cu(II) sites that distorts the framework, keeping the crystallinity of the material. Perturbation observed upon NH<sub>3</sub> adsorption is analogous to that observed for H<sub>2</sub>O, but noticeably enhanced. When the adsorption of ammonia occurs in humid conditions, a time-dependent, much deeper modification of the system is observed by all of the considered techniques. On a methodological ground, it is worth noticing that we used the optimization of XANES spectra to validate the bond distance obtained by EXAFS.



## 1. INTRODUCTION

Metal organic frameworks (MOFs) are crystalline nanoporous materials comprised of two basic structural building units, transition metal ions, or small metal-containing clusters, and connecting polyfunctional organic ligands such as di- or tricarboxylic acids.<sup>1–8</sup> These materials are characterized by a crystalline three-dimensional structure, with very high pore volume and surface area. This hybrid architecture opens the possibility to design and synthesize a great variety of new porous materials, which are in principle able to display novel functionalities that are potentially exploitable for a number of applications in catalysis,<sup>9–19</sup> gas sorption, storage, and separation by selective adsorption.<sup>20–31</sup>

Among the several hundred different MOF structures, Cu<sub>3</sub>(BTC)<sub>2</sub>(H<sub>2</sub>O)<sub>3</sub> (BTC = benzene 1,3,5-tricarboxylate), also known as HKUST-1,<sup>32</sup> is one of the most investigated and among the first commercially available representatives of this class of organic–inorganic hybrid materials, featuring specific adsorption,<sup>33–36</sup> magnetic,<sup>37</sup> and catalytic properties.<sup>38</sup> HKUST-1 is characterized by so-called paddle-wheel units formed by four carboxylate groups coordinating two anti-ferromagnetically coupled Cu(II) ions. The Cu(II) dimers are connected by the BTC linker molecules to form a three-dimensional porous network; water molecules are weakly bound to the residual axial binding site of the Cu(II) ions. These axial water molecules can be easily removed from the Cu(II) dimers by heating at moderate temperature in vacuo to form structurally well-defined accessible Lewis acid copper sites

available for chemisorptions of molecules having basic character.<sup>35,36</sup> In particular, the present contribution is devoted to study the strong adsorption of ammonia basic molecule at room temperature.<sup>39–43</sup>

Ammonia capture is a problem that has some technological relevance. As an example, the biogas produced from anaerobic digestion of biowaste (i.e., animal manure) is mainly composed of methane and carbon dioxide, but also contains some impurity gases, such as ammonia, that has to be removed from the biogas prior to its energy application.<sup>44</sup> Nature has developed complex enzymes able to selectively bind NH<sub>3</sub> molecules;<sup>45</sup> HKUST-1 porous MOF can be considered as a promising synthetic counterpart.<sup>32,39–42,46</sup> The potential of HKUST-1 in ammonia removal from contaminated air streams was reported many years ago by Chui and co-workers.<sup>32</sup> The reaction of ammonia with the individual building blocks of Cu<sub>3</sub>(BTC)<sub>2</sub>, that is, Cu(II) ion and BTC, is well-known. In aqueous solution, Cu(II) ion, in the presence of limited ammonia, is initially converted to Cu(OH)<sub>2</sub>; however, copious amounts of ammonia eventually yield [Cu(NH<sub>3</sub>)<sub>4</sub>]<sup>2+</sup>. Carboxylic acids initially form the ammonium salt, which, with sufficient heating, can be pyrolyzed to their corresponding amides. Peterson et al.<sup>39</sup> states that HKUST-1 reacts with ammonia to form a presumed diammine–copper(II) complex

Received: June 12, 2012

Revised: July 27, 2012

Published: August 3, 2012



under dry conditions and, under humid conditions, a Cu(OH)<sub>2</sub> species and (NH<sub>4</sub>)<sub>3</sub>BTC. Nitrogen adsorption, XRPD, and NMR testing of fresh and exhausted samples all provided evidence for the permanent loss of structure and/or porosity, with samples challenged with ammonia under humid conditions undergoing the largest change. Although the porosity of the material is destroyed, the resulting capacity of the exhausted samples for ammonia is indicative of an extended reactive network consistent with that of the copper(II) complex products.

Herein, we present new details on the adsorption properties of HKUST-1 toward ammonia by applying a multitude of characterization techniques (XRPD, XAFS, IR, DRUV-visible–NIR, and EPR).

## 2. EXPERIMENTAL SECTION

**2.1. Sample Preparation.** HKUST-1 sample was purchased from Sigma-Aldrich. The dehydrated form of HKUST-1 has been obtained upon activation in high vacuum for 1 h at 423 K. Rehydration of the samples was obtained upon contacting the powder with the vapor pressure of water at room temperature: these conditions are significantly milder than those experienced by Kuesgen et al.<sup>47</sup> where HKUST-1 was immersed in deionized water and heated at 323 K for 24 h. As-prepared (rehydrated) and dehydrated samples were exposed to an ammonia equilibrium pressure of 60 mbar. The adsorption of both water and ammonia was carried out at room temperature. EXAFS spectroscopy testifies that adsorption of water vapor pressure and of 60 mbar of NH<sub>3</sub> results in a 1:1 Cu:adsorbate ratio. A large amount of sample was subjected to the same treatment and further separated in different fractions, which were measured by XRPD, XAFS, DRUV-visible, and IR. This method guarantees that the same sample is measured by different techniques.

**2.2. Structural Characterization: XRPD and XAFS.**  
**2.2.1. XRPD Measurements.** X-ray powder diffraction (XRPD) patterns have been collected with a PW3050/60 X'Pert PRO MPD diffractometer from PANalytical working in Debye–Scherrer geometry, using as source the high power ceramic tube PW3373/10 LFF with a Cu anode equipped with Ni filter to attenuate K<sub>β</sub> and focused by X-ray mirror PW3152/63. Scattered photons have been collected by a RTMS (real time multiple strip) X'celerator detector. The samples have been measured as powders inside a 0.8 mm boronsilicate capillary filled in a glovebox and sealed in inert atmosphere, to prevent contamination from moisture.

**2.2.2. XAFS Measurements.** X-ray absorption experiments, at the Cu K-edge (8979 eV), were performed at the BM26B beamline of the ESRF facility (Grenoble, France).<sup>48,49</sup> The white beam was monochromatized using a Si(111) double crystal; harmonic rejection was performed by detuning the crystals at 20% of the rocking curve. The samples were prepared in the form of a pellet, with the thickness optimized to obtain an edge jump of ca. 1, and an absolute  $\mu\chi$  of ca. 1.5. The same pellet was activated and successively treated with NH<sub>3</sub> inside a devoted cell equipped with kapton windows, which allows to perform *in situ* measurements.<sup>50</sup> XAS measurements were performed in transmission mode, using two ionization chambers to monitor the intensity of incident  $I_0$  and transmitted  $I_1$  beams. The chambers were filled with 1 atm of mixed gases (N<sub>2</sub> 15%, He 85% for  $I_0$  and N<sub>2</sub> 70%, He 30% for  $I_1$ ), resulting in 10% and 50% of absorption, respectively. Energy calibration was checked using a Cu metal foil positioned

after the second ionization chamber ( $I_1$ ) and measured using a third ionization chamber ( $I_2$ ), as described elsewhere.<sup>51</sup> The pre-edge region of the XAS spectrum was acquired with an energy step of 10 eV and an integration time of 1 s/point. The edge region was collected using an energy step of 0.2 eV and an integration time of 5 s/point. The EXAFS part of the spectra was collected with a variable sampling step in energy, resulting in  $\Delta k = 0.05 \text{ \AA}^{-1}$ , up to  $18 \text{ \AA}^{-1}$ , with an integration time that linearly increases with  $k$  from 5 to 25 s/point to account for the low signal-to-noise ratio at high  $k$  values. The extraction of the  $\chi(k)$  function was performed using the Athena program.<sup>52</sup> For each sample, four consecutive EXAFS spectra have been collected, and corresponding  $k^3$ -weighted  $\chi(k)$  functions have been averaged before data analysis, as described elsewhere,<sup>53</sup> and Fourier transformed in the  $\Delta k = 2.0\text{--}16.0 \text{ \AA}^{-1}$  range. The fits of the EXAFS spectra measured for the as-prepared, activated, and activated + NH<sub>3</sub> HKUST-1 were performed in R-space in the  $\Delta R = 1.0\text{--}5.0 \text{ \AA}$  range, resulting in 35 independent points ( $2\Delta k\Delta R/\pi > 35$ ). Because of the complexity of the structure,<sup>36,54</sup> more than 50 single scattering (SS) and multiple scattering (MS) paths were included in the fit. To limit the number of optimized variables, all paths have been optimized with the same amplitude factor ( $S_0^2$ ) and with the same energy shift parameter ( $\Delta E$ ). Phases and amplitudes have been calculated by FEFF6 code,<sup>55</sup> adopting as input the structure obtained from a previous XRD refinement.<sup>32,36</sup>

XANES spectra of the hydrated MOF have been simulated using FEFF8.4 code,<sup>56</sup> adopting as input geometry the XRPD structure<sup>32</sup> and cutting a cluster centered on one of the Cu atoms with a radius of 6 Å around it. For a further improvement of the simulations, an optimization of geometrical parameters was performed exploiting FitIt software.<sup>57</sup> The simulation of the dehydrated sample was obtained removing the water molecules from the previous cluster, while for the sample in interaction with ammonia the H<sub>2</sub>O molecules were substituted by two NH<sub>3</sub> ones. In both cases, the structure was optimized to match the experimental spectrum as described for the hydrated case.

In all cases, calculations for the absorption spectra and densities of states have been done using the muffin-tin potential and the Hedin–Lundqvist exchange correlation, taking care of the presence of a core hole in a self-consistency scheme (for the self-consistent calculations, a radius of 4 Å has been used). To take into account the experimental broadening, an imaginary potential  $V_i = 1.0 \text{ eV}$  has been introduced. Although quadrupole transitions are much weaker than the dipole ones, their contribution has been considered in calculations.

**2.3. IR Spectroscopy.** IR spectra have been collected in both mid-IR region (3800–400 cm<sup>-1</sup>) and far-IR region (600–100 cm<sup>-1</sup>). IR spectra in the mid-IR region have been collected in ATR (Attenuated Total Reflectance) mode, by using a Bruker Alpha instrument equipped with an ATR accessory (diamond crystal), and placed inside the glovebox; the spectra have been collected at a resolution of 4 cm<sup>-1</sup>. It is worth noticing that the ATR acquisition mode allows one to collect IR spectra on pure samples in the powdered form without necessity to make a pellet using KBr as diluent (which unavoidably contains some water). This is an advantage when handling samples sensitive to moisture, as in our case. Far-IR spectra have been collected at a resolution of 4 cm<sup>-1</sup> on a Bruker Vertex 70 instrument, equipped with a Si beam splitter and a far-IR DTGS detector. The samples have been diluted in paraffin.

**2.4. UV–Visible–NIR Spectroscopy.** UV–vis–NIR spectra have been collected in diffuse reflectance (DR) mode on a Cary5000 Varian spectrophotometer equipped with a reflectance sphere. All of the samples have been measured in the powdered form inside a homemade cell having an optical bulb (suprasil quartz) and allowing one to perform measurements in controlled atmosphere.

**2.5. EPR Measurements.** CW EPR spectra were recorded on a Bruker EMX spectrometer operating at X-band frequencies and equipped with a cylindrical cavity operating at a 100 kHz field modulation. The spectra have been recorded at 10 mW microwave power. The spectra processing was performed with software provided by Bruker, while for computer simulation the EPRsim32 program was used.<sup>58</sup>

Pulse EPR experiments were performed on an ELEXYS 580 Bruker spectrometer (at microwave frequency 9.76 GHz) equipped with a liquid-helium cryostat from Oxford Inc. All experiments were performed at 10 K. The magnetic field was measured with a Bruker ER035 M NMR Gaussmeter.

Electron–spin–echo (ESE) detected EPR experiments were carried out with the pulse sequence:  $\pi/2-\tau-\pi-\tau$ -echo, with microwave pulse lengths  $t_{\pi/2} = 16$  ns and  $t_{\pi/2} = 32$  ns and a  $\tau$  value of 200 ns. Hyperfine sublevel correlation (HYSCORE) experiments<sup>59</sup> were carried out with the pulse sequence  $\pi/2-\tau-\pi/2-t_1-\pi-t_2-\pi/2-\tau$ -echo with microwave pulse length  $t_{\pi/2} = 16$  ns and  $t_\pi = 16$  ns. The time intervals  $t_1$  and  $t_2$  were varied in steps of 8 ns starting from 100 to 3300 ns. Two different  $\tau$  values were chosen ( $\tau = 104$  and 172 ns). An eight-step phase cycle was used to eliminate unwanted echoes.

The time traces of the HYSCORE spectra were baseline corrected with a third-order polynomial, apodized with a Hamming window, and zero filled. After two-dimensional Fourier transformation, the absolute value spectra were calculated. The spectra were added for the different  $\tau$  values to eliminate blind-spot effects. The HYSCORE spectra were simulated using the EasySpin package.<sup>60</sup>

### 3. RESULTS AND DISCUSSION

**3.1. XRPD Analysis.** The XRPD pattern of as-synthesized hydrated HKUST-1 (blue curve in Figure 1) confirms the crystalline nature of the sample and the absence of any extra phase.<sup>32,36</sup> Upon dosage of ammonia on hydrated HKUST-1, the XRPD pattern is strongly modified (orange curve in Figure 1), indicating a significant distortion of the lattice, which however does not undergo a complete amorphization. After prolonged exposure time, a further modification of the diffraction features, along with an overall broadening of the peaks, is observed (Figure 1, purple curve).<sup>39</sup>

The XRPD pattern of the activated sample (pink curve in Figure 1) was previously reported by Prestipino et al.<sup>36</sup> This pattern shows an overall slight shift of the diffraction peaks toward higher  $\theta$ -values if compared to that of the as-prepared material; this observation is compatible with a global contraction of the bond lengths induced by the activation process. Moreover, the dehydration induces a strong intensity enhancement of a diffraction peak in the very low- $\theta$  region, around 6.7°. Surprisingly, if pure dry ammonia is dosed on the activated material, the diffraction pattern (light green curve in Figure 1) is much less perturbed than that obtained by dosing ammonia on the hydrated sample. Nevertheless, comparing this pattern with the one measured for the activated MOF, a slight shift in the peaks positions toward shorter  $\theta$  values is observed, as well as small variations in their relative intensities. The

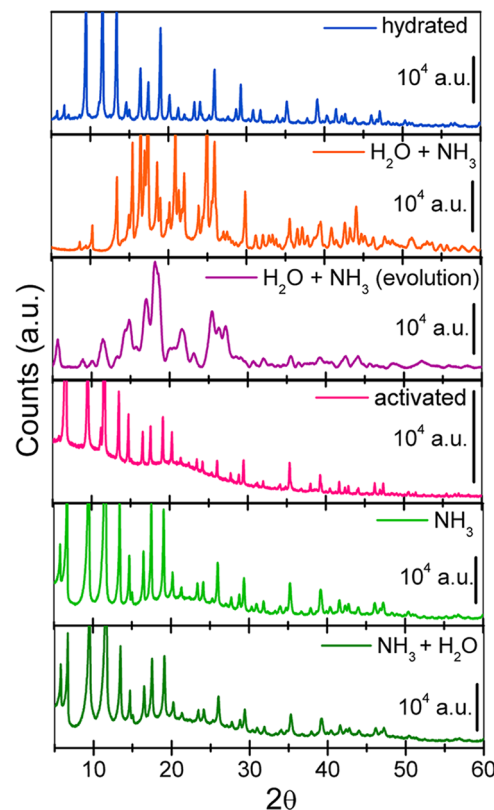


**Figure 1.** XRPD patterns of HKUST-1 in different conditions: as-prepared (hydrated, blue line), after dosage of ammonia on a sample previously contacted with water vapor pressure (orange line), and its evolution after prolonged exposure time in such conditions (purple line), activated sample (pink line, adapted from Prestipino et al.<sup>36</sup>), after pure dry ammonia dosage on the activated sample (light green line), and after contacting with water vapor pressure the sample previously exposed to ammonia in dry conditions (dark green line).

intense peak around 6.7° already observed for the activated material is maintained after interaction with dry NH<sub>3</sub>. The main difference with respect to the pattern of the activated sample is the appearance of a peak around 5.8°, which was not present at all in the pattern of the activated material. Therefore, it should be concluded that HKUST-1 framework is only slightly perturbed upon NH<sub>3</sub> adsorption and goes back to a situation similar to that characteristic of hydrated material, with a slight generalized lengthening of the bond distances. Finally, the XRPD pattern does not change when H<sub>2</sub>O is dosed on the sample precontacted with NH<sub>3</sub> (Figure 1, dark green curve). The XRPD data shown in Figure 1 demonstrate that NH<sub>3</sub> alone affects the crystalline structure of the dehydrated HKUST-1 only very slightly, whereas in combination with H<sub>2</sub>O it causes a drastic change in the structure, up to the complete amorphization of the sample. However, the effect is observed only when H<sub>2</sub>O is dosed first, and NH<sub>3</sub> later.

The quality of the XRPD data shown in Figure 1 is not enough to allow a structure refinement. To gain information on the local environment around copper centers in the absence and in the presence of ammonia, we used Cu K-edge EXAFS spectroscopy.

**3.2. XAS Analysis. 3.2.1. XANES Spectroscopy.** Investigation of the XANES region of the X-ray absorption spectrum can provide detailed information on both the oxidation state and the coordination symmetry of the absorber atom and was

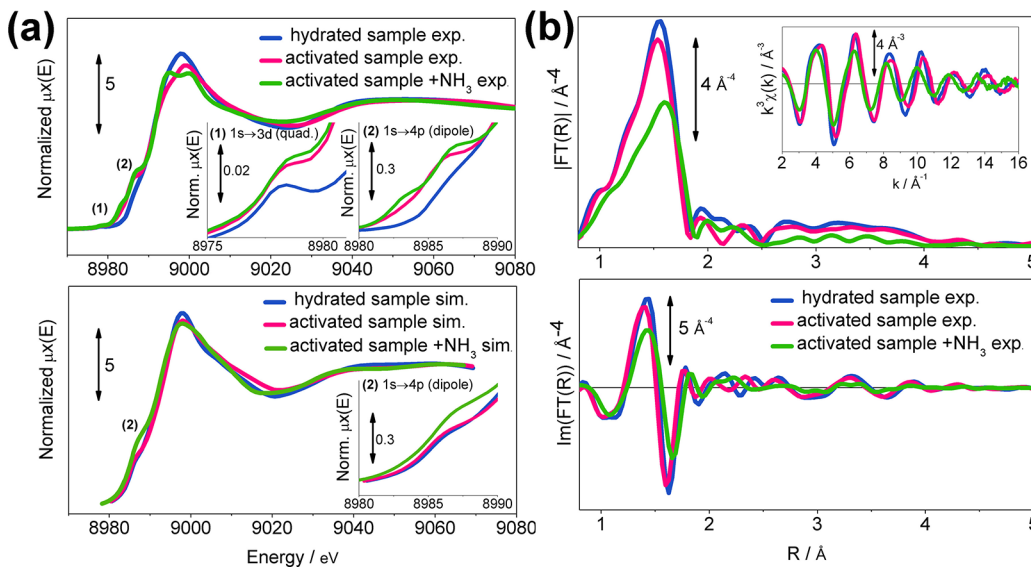


**Figure 2.** (a) Experimental (top panel) and simulated (bottom panel) XANES spectra of HKUST-1 as-prepared (blue line), activated (pink line), and activated + NH<sub>3</sub> (green line). The insets report magnifications of the 1s → 3d quadrupolar transition (1) and of the shakedown 1s → 4p transition (2). (b) Qualitative comparison between experimental EXAFS data for as-prepared and activated HKUST-1, and for the activated sample upon contact with 50 mbar of ammonia. Modulus (top panel) and imaginary part (bottom panel) of the FT of the  $k^3$ -weighted  $\chi(k)$  functions reported in the inset for the as-prepared (blue line), activated (pink line), and activated + NH<sub>3</sub> (green line) sample. The inset in the top part reports the corresponding  $k^3 \chi(k)$  functions.

successfully applied in the structural characterization of several Cu-containing materials.<sup>36,51,61–72</sup> In Figure 2a, top panel, are reported the experimental XANES spectra of HKUST-1 as-prepared (hydrated sample, blue solid line), after activation at 453 K (dehydrated sample, pink solid line), and upon contact with 60 mbar of ammonia at room temperature (green solid line). As pointed out in a previous work,<sup>36</sup> the XANES spectra of the as-prepared and dehydrated sample are typical of Cu(II) species, showing the edge jump at 8990 eV and two characteristic pre-edge peaks at ca. 8976 eV and ca. 8986 eV, labeled as (1) and (2), respectively, in Figure 2a, and separately reported in the insets of the same Figure. Feature (1) is assigned to the very weak 1s → 3d quadrupolar transition, while the shoulder (2) appearing along the white line profile is related to the dipolar shakedown 1s → 4p transition. The simulation of the spectrum of the hydrated material was performed starting from the XRPD structure<sup>32</sup> and optimizing five structural parameters: (i) the Cu–Cu and (ii) Cu–H<sub>2</sub>O bond length, the distance between the Cu atom and the trimesic acid carboxyl groups with a separate optimization of (iii) Cu–O1 and of (iv) Cu–C and Cu–O2 distances (optimized in a correlated way to use only one free parameter), and (v) a general overall contraction or elongation of all of the other distances ( $R_{\text{XANES}} = \alpha R_{\text{XRPD}}$ ).<sup>73</sup> See Figure 3a for the atom notation. The variations in the simulated spectrum introduced by the geometrical distortions have been monitored by using the FitIt software. In conclusion, it has been observed that a variation of Cu–Cu distance resulted in very slight changes in the XANES features, the Cu–H<sub>2</sub>O distance influences the intensity and partially the position in energy of the pre-edge feature (2), and the carbonyl group distances and a possible overall contraction or expansion strongly influence both the intensity and the position of the white line and the shape of the multiple scattering features at higher energies. In the case of the hydrated sample, the best agreement between the simulated curve and experimental data was obtained with a

slight shortening of Cu–H<sub>2</sub>O distance, an elongation of 0.05 Å of both Cu–O1 and a constrain of Cu–C and Cu–O2 distances, corresponding to a shift along the bond axis of the carbonyl groups, and a slight general contraction of all other distances.

Upon water removal, no shift in the absorption edge is observed, providing evidence that no change in oxidation state of the Cu center occurs. However, the XANES spectrum of the activated sample shows (i) a decrease of the white line intensity, and (ii) an increase in the intensity of feature (2), which appears more as a well-separated band than as a white line shoulder. The simulation of the XANES spectrum for the activated sample was performed with the same method previously described for the hydrated sample removing the atoms of the two water molecules, resulting in an optimization with four parameters only. Even without a structural optimization, in the simulated spectra has been observed the same trend noticed on the experimental curves where the decrease of the white line intensity is correlated to the lower coordination number, and the increase of the intensity of feature (2) is ascribable to a lower symmetry of the Cu(II) species. In the simulated curves, this trend is less evident probably because a full description of the asymmetric distortion undergone by the Cu species in the activated sample would require a too high number of parameters to be optimized. The optimization of the bond distances resulted in a slight contraction of the distances between the absorbing Cu atom and carbonyl groups and all other distances, in agreement with the results found by EXAFS fit (see section 3.2.2 and Table 1).

The XANES spectrum of the activated sample after the interaction with NH<sub>3</sub> evidences an additional increase in the intensity and a slight blue-shift of the dipole band (2) assigned to the 1s → 4p transition. Moreover, a new pre-edge peak is observed at ca. 8983 eV. Despite that the edge position is not modified with respect to the as-prepared and activated samples (no change in oxidation state of the metal), the white line is

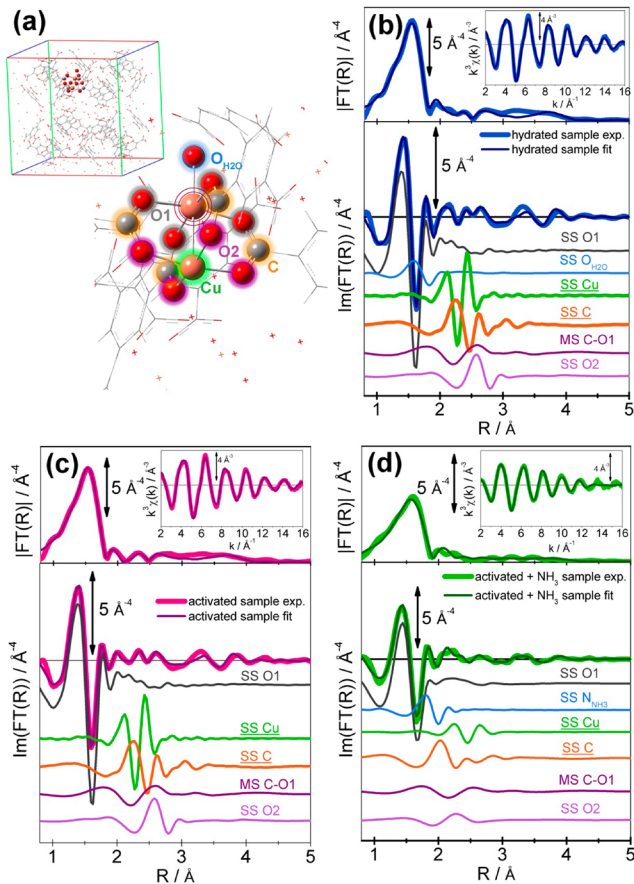


**Figure 3.** (a) Structure of the as-such sample obtained from a previous XRD refinement, and magnification of the cluster used as starting point for the fitting procedure of EXAFS data. Atom color code is the following: Cu pale pink, C gray, O red. The groups of atoms involved in the principal paths contributing to EXAFS signal are labeled and highlighted by different colored halos (oxygen atoms of the trimesic acid carboxyl groups directly coordinated to the  $\text{Cu}_{\text{abs}}$ , O1, gray; oxygen of the water molecule directly coordinated to the Cu absorber,  $\text{O}_{\text{H}_2\text{O}}$ , light blue; second copper atom of the dimer in front of the absorber, Cu, green; the four carbon atoms of the trimesic acid carboxyl groups, C, orange; oxygen atoms coordinated to the not absorber copper site, O2, purple). (b–d) Comparison between experimental and corresponding best fits for the as-such (b), activated (c), and activated +  $\text{NH}_3$  (d) sample. Top panels report the modulus of the FT, while bottom panels show the imaginary parts of the FT, and the principal path contributions to the total signal. For quantitative values of the parameters optimized in the fits, see Table 1.

modified toward a more structured appearance and seems to return toward the shape observed for the hydrated sample. The simulation of the spectrum for the sample after interaction with  $\text{NH}_3$  was performed following the same method adopted for the hydrated material and substituting the water molecules with two  $\text{NH}_3$  molecules. After the optimization of the geometrical parameters, it was observed that the intensity of the pre-edge feature (2) is proportional to the  $\text{Cu}-\text{NH}_3$  distance, which was optimized at 2.3 Å with a considerable elongation with respect to the previous position of the water molecules. Moreover, a splitting of the white line feature, although less evident with respect to the experimental spectra, has been observed after a distortion of carbonyl groups simulated by a slight elongation of  $\text{Cu}-\text{O}1$  distances but a severe shortening of both  $\text{Cu}-\text{C}$  and  $\text{Cu}-\text{O}2$  and all other distances. It is worth noticing that the

deformation introduced to simulate the XANES spectra is in agreement with the results of the EXAFS fit.

**3.2.2. EXAFS Spectroscopy.** The quality of the EXAFS spectra, in terms of S/N ratio, can be checked in Figure 2b (inset in the top panel), where the extracted  $k^3\chi(k)$  functions are reported. EXAFS data analysis was performed up to  $k = 16 \text{ \AA}^{-1}$ , thus obtaining satisfactory structural information up to the third shell of atoms around the Cu absorber, that is, up to atomic distances within a sphere with ca. 5 Å of radius. The corresponding  $k^3$ -weighted Fourier transformed functions, in the 2–16  $\text{Å}^{-1}$  range, are shown in Figure 2b for both the moduli (top panel) and the imaginary parts (bottom panel). The three spectra are dominated by the first shell signal (at ca. 1.5 Å, not corrected in phase); contributions at longer distances are weaker, although the modulation of the imaginary part provides evidence that the experimental signal still contains structural information. The spectrum of the activated sample (pink curves) is very similar to that of the as-prepared sample (blue curves), and only a slight shift toward shorter  $R$ -values and a small decrease of the amplitude of the first shell signal are observed. The shift reveals an overall contraction of the bond distances after thermal activation, in agreement with XRPD data, while the lower intensity of the first shell is a consequence of the reduction of the Cu coordination number (loss of the water molecule coordinated to the Cu atom). The imaginary parts of the FT in the high- $R$  region ( $R > 2.5 \text{ \AA}$ ) are very similar, indicating that after thermal activation the framework of HKUST-1 remains substantially unchanged in a long range, and only the first shell of the Cu-absorber is modified, as expected for dehydration.

The situation is drastically different for the activated sample in interaction with ammonia. The EXAFS spectrum is characterized by a first shell signal weaker and shifted toward longer bond distances, if compared to that of the activated sample. In addition, oscillations of the  $\text{Im}(\text{FT})$  in the high- $R$  range are noticeably damped in amplitude. The interpretation of this experimental behavior requires particular attention. The strong reduction of EXAFS signal might be intuitively ascribed to a great modification of the framework. However, the XRPD results (as well as IR and UV-vis characterization, vide infra) demonstrate that only a slight structural rearrangement occurs upon  $\text{NH}_3$  dosage in absence of water, coherent with the simple  $\text{NH}_3$  coordination to the Cu metal center after dehydration. As will be discussed in detail hereinafter, the lowering of the EXAFS signal amplitude can be explained with a phenomenon of destructive interference among some of the main EXAFS paths involved, already observed in the analysis of the as-such and activated samples, and further intensified after the  $\text{NH}_3$  coordination.

A quantitative analysis of the EXAFS spectrum for the as-prepared sample has been performed starting from the cluster shown in Figure 3a, where the five shells of scatterer atoms giving the main contribution to the FT-transformed EXAFS signal are highlighted by different colored halos and the Cu atom acting as absorber is circled in red ( $\text{Cu}_{\text{abs}}$ ). The first shell includes four equivalent oxygen atoms of the trimesic acid carboxyl groups in square planar geometry (O1) and the oxygen of the water molecule ( $\text{O}_{\text{H}_2\text{O}}$ ) directly coordinated to the Cu absorber. The main contributions at longer distance come from SS paths involving the second copper atom of the dimer (Cu) in front of the absorber, the four carbon atoms of the trimesic acid carboxyl groups (C), the four oxygen atoms coordinated to this second copper site (O2), and, finally, from

**Table 1. Summary of the Parameters Optimized in the Fit of the EXAFS Data (Figure 3b–d) for HKUST-1 Samples As Such, Dehydrated, and after Exposure to 60 mbar of NH<sub>3</sub><sup>a</sup>**

	as such (hydrated)	activated (dehydrated)	activated + NH <sub>3</sub>
independent points	35	35	35
number of variables	14	12	13
R-factor	0.014	0.010	0.018
S <sub>0</sub> <sup>2</sup>	0.99 ± 0.05	0.81 ± 0.03	0.99 ± 0.05
ΔE (eV)	-2.7 ± 0.6	-3.6 ± 0.5	-3.1 ± 0.5
R <sub>O1</sub> (Å)	1.959 ± 0.005	1.934 ± 0.005	2.000 ± 0.004
σ <sup>2</sup> <sub>O1</sub> (Å <sup>2</sup> )	0.0054 ± 0.0007	0.0051 ± 0.0006	0.0094 ± 0.0003
R <sub>O(H<sub>2</sub>O)</sub> or R <sub>N(NH<sub>3</sub>)</sub> (Å)	2.24 ± 0.03		2.31 ± 0.01
σ <sup>2</sup> <sub>O(H<sub>2</sub>O)</sub> or σ <sup>2</sup> <sub>N(NH<sub>3</sub>)</sub> (Å <sup>2</sup> )	0.011 ± 0.006		0.006 ± 0.002
R <sub>Cu</sub> (Å)	2.65 ± 0.02	2.58 ± 0.02	2.80 ± 0.03
σ <sup>2</sup> <sub>Cu</sub> (Å <sup>2</sup> )	0.012 ± 0.002	0.015 ± 0.003	0.013 ± 0.03
R <sub>C</sub> (Å)	2.88 ± 0.02	2.84 ± 0.02	2.56 ± 0.03
σ <sup>2</sup> <sub>C</sub> (Å <sup>2</sup> )	0.008 ± 0.002	0.008 ± 0.001	0.013 ± 0.005
R <sub>O2</sub> (Å)	3.14 ± 0.03	3.07 ± 0.03	2.82 ± 0.04
σ <sup>2</sup> <sub>O2</sub> (Å <sup>2</sup> )	0.021 ± 0.005	0.024 ± 0.005	0.03 ± 0.01
α	-0.012 ± 0.004	-0.021 ± 0.004	-0.003 ± 0.002
σ <sup>2</sup> (Å <sup>2</sup> )	0.009 ± 0.002	0.009 ± 0.002	0.016 ± 0.002

<sup>a</sup>All of the fits were performed in *R*-space in the Δ*R* = 1.00–5.00 Å range, over *k*<sup>3</sup>-weighted FT of the  $\chi(k)$  functions performed in the 2–16 Å<sup>-1</sup> interval. A single ΔE<sub>0</sub> and a single S<sub>0</sub><sup>2</sup> have been employed to parametrize all SS and MS paths. In the activated + NH<sub>3</sub> case, the amplitude S<sub>0</sub><sup>2</sup> was fixed to the value refined for hydrated sample (S<sub>0</sub><sup>2</sup> = 0.99 ± 0.05), where the Cu center is expected to have the same coordination number. For all paths, the degeneration (coordination number for SS paths) has been fixed to the values expected from the structure refined by single-crystal XRD.<sup>32</sup> This holds also for the number of water (column 2) and ammonia (column 4) adsorbed on the Cu(II) site (*N*<sub>ads</sub>), which was fixed to unit in both cases. To check the adsorption stoichiometry, additional fits were performed optimizing also the number of adsorbed molecules: *N*<sub>ads</sub> was 1.04 ± 0.08 and 1.0 ± 0.1 for H<sub>2</sub>O and NH<sub>3</sub>, respectively.

Cu<sub>abs</sub>–C–O1 MS paths. For all of these scattering paths, the distance and the Debye–Waller factor have been fitted independently. The remaining SS and MS were modeled describing length variation ΔR<sub>i</sub> and Debye–Waller factor σ<sup>2</sup><sub>i</sub> of the *i*th path according to the following relations: ΔR<sub>i</sub> = αR<sup>eff</sup><sub>i</sub> and σ<sup>2</sup><sub>i</sub> = σ<sup>2</sup>(R<sup>eff</sup><sub>i</sub>/R<sub>O1</sub>)<sup>1/2</sup>, that is, considering the possibility of an overall isotropic contraction/dilatation of the distances (parameter α) and assuming a Debye–Waller factor increasing proportionally to the square root of the path effective length R<sup>eff</sup><sub>i</sub>. This approach has already been used to limit the overall number of optimized parameters in systems where a high number of SS and MS paths contributes significantly to the overall signal such as metal-oxides<sup>73–77</sup> and MOFs.<sup>31,54,78–84</sup> Finally, single ΔE and S<sub>0</sub><sup>2</sup> values common to all of the paths have been fitted. The complete fitting model needed 14 independent parameters, see Table 1, and represents an improvement of the EXAFS study by Prestipino et al.<sup>36</sup> The same structural model was adopted for the analysis of the dehydrated sample, before and after interaction with ammonia. In the former case, the paths involving the water molecule (O<sub>H<sub>2</sub>O</sub>) were excluded (resulting in 12 independent parameters), whereas in the latter no changes were done, because O atom (of H<sub>2</sub>O) and N atom (of NH<sub>3</sub>) are not distinguishable by EXAFS. In that case, the amplitude factor S<sub>0</sub><sup>2</sup> was fixed to the value obtained for the as-prepared sample (resulting in 13 independent parameters).

Figure 3b–d shows the experimental signals for the three investigated samples and the different paths contribution to the Imm(FT), whereas Table 1 summarizes the optimized parameters. In all three cases, the simulated EXAFS spectra well reproduce the experimental curves, as proved by the *R*-factor values that are always lower than 5%. In many cases, different scattering paths contributing in the same distance range are characterized by Imm(FT) in antiphase; their contributions to the overall signal are consequently canceled,

because of destructive interference. This is in particular evident in the first shell region for the dehydrated sample in interaction with NH<sub>3</sub> (Figure 3d), where the SS N<sub>NH<sub>3</sub></sub> path is in partial antiphase with the SS C contribution, and the MS C–O1 and SS O2 contributions are characterized by a partial mutual depletion, globally resulting in a drastic erosion of the EXAFS signal. Although rare, such a “cancellation” effect has already been observed in EXAFS studies on other materials: particularly relevant is the strong amplitude reduction of the second shell peak in Ga K-edge EXAFS spectra of In<sub>x</sub>Ga<sub>1-x</sub>As semiconductor solid solutions when *x* is close to 0.5.<sup>85,86</sup>

The optimized parameters resulting from the fit are summarized in Table 1. For the as-prepared sample, almost all of the optimized distances are within their associated error equal to the ones extracted from single-crystal XRD data of Chui et al.<sup>32</sup> or slightly longer. Upon activation, a generalized contraction of the bond lengths is observed, as was already reported by Prestipino et al.<sup>36</sup> This contraction, particularly evident for the Cu<sub>abs</sub>–Cu distance, is also testified by a negative value of the contraction/expansion parameter α = -0.021 ± 0.004. The Debye–Waller factors assume physically plausible values for all of the different shells of atoms. Only the value for the oxygen atoms coordinated to the non-absorber copper site (O2) is high because of a high static disorder term, due to the higher heterogeneity of the corresponding sites, not directly bonded to Cu<sub>abs</sub>.

When the dehydrated sample is treated with ammonia, an increase in the Cu<sub>abs</sub>–O1 average bond distance is observed (R<sub>O1</sub> = 2.000 ± 0.004 Å), accompanied by an increase in the Debye–Waller factor σ<sup>2</sup><sub>O1</sub>, which goes from ca. 0.005 to 0.009 Å<sup>2</sup>. The optimized Cu<sub>abs</sub>–N<sub>NH<sub>3</sub></sub> bond distance value obtained from the fit is of (2.31 ± 0.01) Å, with a Debye–Waller value σ<sup>2</sup><sub>N(NH<sub>3</sub>)</sub> = (0.006 ± 0.002) Å<sup>2</sup>. Therefore, EXAFS data provide evidence that adsorption of ammonia on the coordinative vacancy of Cu(II) in dehydrated HKUST-1 occurs without the

break of any first shell Cu–O1 bonds, which just undergo an elongation of  $\sim 0.050$  Å to accommodate the NH<sub>3</sub> molecule. This elongation is more than double that needed to accommodate the water molecule; see Table 1. Additional structural distortions involve the higher shells, in particular, (i) the Cu<sub>abs</sub>–Cu bond is elongated  $\sim 0.15$  Å, and (ii) the Cu–C and Cu–O2 bond lengths are slightly contracted. Finally, it is worth noticing that fit results are affected by a higher degree of incertitude with respect to the as-such and activated cases, due to the lower signal-to-noise ratio and the possibility of different structural rearrangements resulting in the same signal suppression. A general increase of the DW values associated to C and O2 shells, as well as of the  $\sigma^2$  Debye–Waller used to model SS and MS paths whose contribution to EXAFS signal is minor, is found.

### 3.3. Optical Properties: DRUV–Vis Spectroscopy.

Upon activation, the color of HKUST-1 changes from light cyan (Figure 4a) to navy blue (Figure 4b, first tube). To explain this behavior, a change in the coordination sphere of copper species should be invoked, as the color is associated with d–d transitions of Cu(II) ions. The DRUV–vis spectra of the as-synthesized and activated samples are reported in Figure 4c

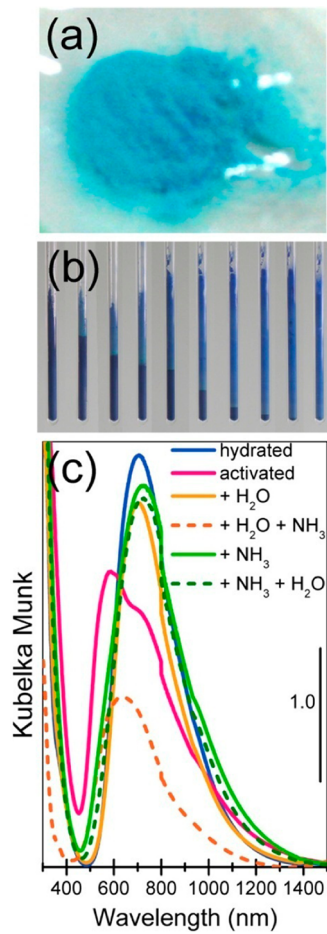


**Figure 4.** (a) Picture of hydrated HKUST-1 sample. (b) Sequence of pictures showing the HKUST-1 color evolution upon NH<sub>3</sub> dosage and progressive advance of the NH<sub>3</sub> front, starting from the activated material (first tube). (c) DRUV–vis spectra of HKUST-1 as-prepared (blue line), activated (pink line), activated + H<sub>2</sub>O and successively + NH<sub>3</sub> (orange solid and dashed line, respectively), and activated + NH<sub>3</sub> and successively + H<sub>2</sub>O (green solid and dashed line, respectively).

(blue and pink lines, respectively). The spectrum of the fresh sample (blue curve) shows (i) an edge around 350 nm due to a ligand to metal charge transfer (LMCT) transition from oxygen to copper atoms; and (ii) a band centered at about 705 nm, characteristic of the d–d transition for Cu(II) species in a distorted octahedral local geometry. The distortion of the octahedral geometry accounts for the high intensity of the band that should be otherwise dipole-forbidden.

The main effect of activation at 423 K (pink curve) is the appearance of a high-energy shoulder in the d–d band at around 585 nm. At the same time, a red shift of the maximum, previously observed at 705 nm, to 745 nm and of the absorption associated with the LMCT transition is observed. The increase of the fraction of absorbed visible light causes a complete darkening of the material, which changes from light cyan to navy blue. The change in the d–d region is ascribed to the activation of new available d–d transitions due to a loss of degeneracy in d levels produced by a change in the symmetry around copper. Coming to the high-energy part of the UV–vis spectrum, the LMCT edge shift is explained as a consequence of the change of (i) the hydration conditions of the carboxylated group and (ii) the coordination sphere of copper ions.<sup>36</sup> Upon H<sub>2</sub>O vapor pressure dosage on the activated sample, the original spectrum is restored (orange solid curve), demonstrating the reversibility of the process.<sup>36</sup> If pure dry ammonia is dosed on the activated material, the spectrum (green solid curve) is quite similar to that of the hydrated sample, apart for a slight red shift of the d–d band to 725 nm. This small shift is sufficient to cause a color change, as demonstrated by the sequence of photographs reported in Figure 4b, collected at increasing NH<sub>3</sub> contact time.

On the contrary, the dosage of ammonia on a sample previously contacted with water vapor pressure causes a big change in the spectrum (see orange dashed line), providing evidence that the coordination sphere of Cu(II) is strongly perturbed. The effect of water after pure ammonia adsorption has been considered too, and the resulting spectrum is almost unperturbed (see green dashed curve). These results are in good agreement with those of XRPD.

### 3.4. Vibrational Properties: IR Spectroscopy.

The vibrational properties of HKUST-1 in the mid-IR range have been studied by collecting the spectra in ATR mode (see Figure 5a). In this frequency range, the spectra of hydrated sample HKUST-1 are dominated by the vibrational modes of the BTC linker. In particular, the IR absorption bands in the 1700–1500 and 1500–1300 cm<sup>-1</sup> ranges are due to  $\nu_{\text{asym}}(\text{C}=\text{O}_2)$  and  $\nu_{\text{sym}}(\text{C}=\text{O}_2)$  stretching modes, respectively; IR bands around 1450 cm<sup>-1</sup> are due to a combination of benzene ring stretching and deformation modes; whereas IR absorption bands around 700 cm<sup>-1</sup> are due to  $\nu(\text{C}-\text{H})$  bending mode. Only the IR absorption band centered at 493 cm<sup>-1</sup> is due to a vibrational mode directly involving the Cu center, and it will be discussed later.

The mid-IR spectrum of HKUST-1 does not change upon dehydration (only the broad IR absorption band centered at 3300 cm<sup>-1</sup> disappears), neither upon adsorption of NH<sub>3</sub> (apart a slight broadening of most of the IR absorption bands). On the contrary, the spectrum greatly changes when ammonia is dosed on the hydrated sample. In particular, in the 1700–1500 cm<sup>-1</sup> range, only two distinct absorption bands are observed at 1610 and 1544 cm<sup>-1</sup>; the IR bands in the 1500–1300 cm<sup>-1</sup> region are slightly red-shifted; new IR absorption bands appear at 1250, 1213, and 708 cm<sup>-1</sup>. Although further investigation is

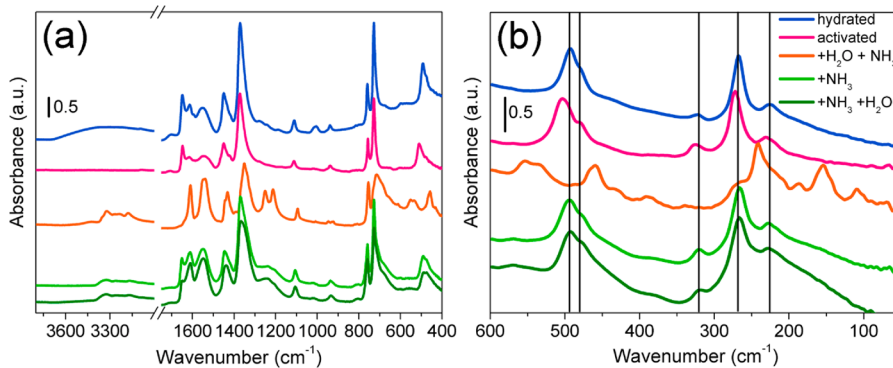


**Figure 5.** Mid-IR (ATR mode) (a) and far-IR (transmittance mode) (b) spectra of HKUST-1 as-prepared (blue line), activated (pink line), activated + H<sub>2</sub>O and + NH<sub>3</sub> (orange line), activated + NH<sub>3</sub> (light green line), and successively + H<sub>2</sub>O (dark green line).

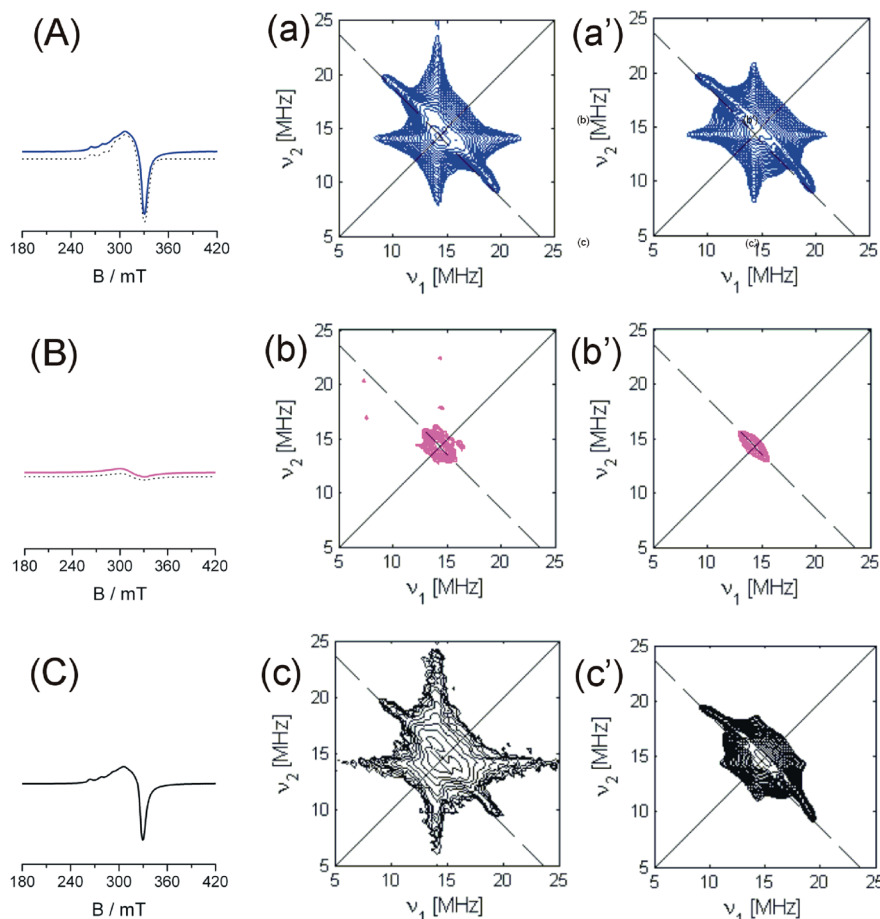


**Figure 6.** (A–C) Experimental (solid lines) and simulated (dotted lines) X-band CW-EPR spectra of hydrated (blue line), dehydrated (pink line), and rehydrated (black line) HKUST-1. (a–c) Experimental <sup>1</sup>H HYSCORE spectra. (a'–c') Corresponding computer simulations. All spectra were recorded at 10 K. The HYSCORE spectra were taken at observer position  $B_0 = 336$  mT, corresponding to the  $g_{\perp}$  component of the field swept spectrum. Two spectra measured with  $\tau = 104$  and 172 ns are added together after Fourier transform.

necessary to assign precisely the new IR absorption bands, the mid-IR spectrum of the hydrated sample after interaction with ammonia is clearly in favor of a big structural change, in agreement with all of the data discussed above.

IR spectra in the far-IR region (see Figure 5b) are much more informative, because in the 600–50 cm<sup>-1</sup> range the vibrational modes directly involving Cu(II) species are present. The same frequencies range was previously explored in detail by means of Raman spectroscopy<sup>36</sup> for the hydrated and activated sample. The far-IR spectrum of the hydrated sample

(blue curve) shows two main absorption regions, around 500 cm<sup>-1</sup> (main peak at 493 cm<sup>-1</sup> and shoulder at 480 cm<sup>-1</sup>) and around 280 cm<sup>-1</sup> (three absorption bands centered at 321, 269 (the most intense), and 226 cm<sup>-1</sup>). Following the previous interpretation,<sup>36</sup> the IR absorption bands around 500 cm<sup>-1</sup> are assigned to Cu–O stretching modes, while the absorption bands at lower frequency are due to vibrational modes involving the Cu–Cu stretching of the two Cu(II) ions of the [Cu<sub>2</sub>C<sub>4</sub>O<sub>8</sub>] framework cage. Upon activation, both the IR absorption band at 493 cm<sup>-1</sup> and the three bands at lower

frequency blue-shift to 504, 326, 273, and 231  $\text{cm}^{-1}$ , respectively. This observation reveals an increase in rigidity of the metallorganic framework structure, in agreement with the shortening of the Cu–O and Cu–Cu bonds obtained by EXAFS. Finally, when ammonia is adsorbed on the dehydrated sample (light green spectrum), the far-IR spectrum comes back to that of the hydrated sample, whereas interaction of ammonia on a hydrated sample causes a drastic change of the overall spectrum.

**3.5. EPR Characterization.** The CW-EPR spectrum of hydrated HKUST-1 is characterized by a typical anisotropic powder pattern characteristic of hydrated Cu(II) ions having an electron spin  $S = 1/2$  and interacting with the  $I = 3/2$  nuclear spin of the copper nuclei (Figure 6A, blue line). The parameters derived from the simulation (Figure 6A, dotted line) are listed in Table 2 and are in agreement with those previously reported by Pöppel et al.<sup>87–90</sup> on the same system.

**Table 2. Spin Hamiltonian Parameters of Cu(II) Species in HKUST-1 Obtained by Computer Simulation of the Spectra in Figure 6**

	g tensor	hyperfine tensor ${}^{\text{Cu}}\text{A}/\text{MHz}$
type A Cu(II)	$g_{\parallel} = 2.374 \pm 0.001$	$A_{\parallel} = 456 \pm 3$
	$g_{\perp} = 2.089 \pm 0.007$	$A_{\perp} = 73 \pm 12$
type B Cu(II)	$g = 2.17 \pm 0.02$	

The spectrum consists of two superimposed signals, indicated in Table 2 as type A Cu(II) and type B Cu(II). The spin Hamiltonian parameters of type A are typical for isolated Cu(II) hydrated monomers, while the second species (type B), characterized by a broad unresolved line, with  $\Delta B^{\text{PP}} = 30 \text{ mT}$  and  $g_{\text{av}} = 2.17$  has been assigned to interacting Cu(II) species.<sup>87</sup>

Quantitative evaluation of the monomeric copper species in the hydrated sample has been obtained by comparison of the CW EPR spectral intensity with that of a standard solution of copper acetylacetone. The estimated percentage of isolated Cu(II) ions is found to be about 6% of the overall copper ions in the sample. In agreement with earlier literature reports,<sup>87</sup> we assign such isolated ( $S = 1/2$ ) Cu(II) species to residual extra-framework monomeric Cu(II) ions, which have not been incorporated as  $[\text{Cu(II)}]_2$  dimers in the  $\text{Cu}_3(\text{BTC})_2$  network.

Upon dehydration at 423 K under vacuum, the sample develops a navy blue color and shows the EPR spectrum of Figure 6B (pink line). The signal due to the monomeric Cu(II) ions is drastically reduced in intensity, while the broad signal due to interacting copper species (type B) becomes evident. The overall decrease of the EPR spectral intensity is about 20% of the hydrated spectrum (blue line). The original spectrum can be restored by hydration of the sample (Figure 6C, black line).

To investigate more deeply the effects caused by dehydration and rehydration of the sample and in the effort of better characterizing the local coordination environment of the Cu(II) monomers, hyperfine sublevel correlation (HYSCORE) measurements were carried out.

The HYSCORE spectra recorded at observer position  $B_0 = 336 \text{ mT}$ , corresponding to the Cu(II) perpendicular feature, are reported in Figure 6a–c (spectra taken at a magnetic field setting corresponding to the parallel position are reported as Supporting Information). The spectrum of the hydrated material (Figure 6a) is characterized by a pronounced broad proton ridge centered at  $(\nu_{\text{H}}, \nu_{\text{H}})$  with maximum extension of

about 11.8 MHz, stemming from the superhyperfine interaction between the unpaired electron in the  $d_{x^2-y^2}$  Cu(II) orbital and a nearby proton. The experimental spectrum can be simulated (Figure 6a') using the parameters reported in Table 3. These values are typical for water molecules equatorially coordinated to the Cu(II) ions<sup>91</sup> and are in line with those found for the  $\text{Cu}(\text{H}_2\text{O})_6^{2+}$  complex.<sup>92</sup>

**Table 3. Spin Hamiltonian Parameters Deduced from Simulation of the HYSCORE Spectra of Figure 6a, b, and c**

proton species interacting with Cu(II)	${}^{\text{H}}\text{a}_{\text{iso}}/\text{MHz}$	${}^{\text{H}}\text{T}/\text{MHz}$	$\alpha; \beta; \gamma/\text{deg}$
A	$0.2 \pm 0.5$	$5.8 \pm 0.5$	$0;70;0 \pm 0;10;0$
B	$0.4 \pm 0.5$	$1.4 \pm 0.5$	$0;60;0 \pm 0;10;0$

The simulation analysis indicates that the experimental spectrum is best reproduced by considering a second interacting proton with maximum coupling of about 3 MHz due to remote protons, weakly interacting with Cu(II) monomers.

The HYSCORE spectrum of the dehydrated sample, recorded at the same observer position, is reported in Figure 6b. As a consequence of the dehydration treatment, the pronounced ridge with maximum coupling 11.8 MHz disappears, and only the small proton ridge with maximum extension of about 3 MHz is observed. Admission of water onto the dehydrated sample restores the original proton ridge (Figure 6c). This is in agreement with the CW-EPR spectrum reported in Figure 6C.

The hydration–dehydration behavior of monomeric Cu(II) species in HKUST-1 is reminiscent of that of hydrated cupric Cu(II) ions in zeolites where the same phenomenon, that is, an intensity drop of Cu(II) EPR spectra upon thermal treatment in vacuo and subsequent restoring by simple water adsorption at room temperature, is well-known.<sup>64</sup> This effect, often called “self-reduction” process, has been interpreted in the case of zeolites in terms of a proper reduction mechanism involving the formation via different pathways of cuprous (diamagnetic) ions ( $\text{Cu}^+$ ).<sup>93,94</sup> This interpretation was however challenged by Lo Jacono and co-workers,<sup>95</sup> who suggested that the loss of intensity of the EPR signal has to be ascribed to changes in the coordination of Cu(II) ions, which become EPR inactive, without invoking the formation of  $\text{Cu}^+$  ions. This second mechanism was later verified by a multitechnique approach.<sup>64</sup> Our experiments indeed show that this second mechanism is appropriate to describe the behavior of isolated Cu(II) ions in  $\text{Cu}_3(\text{BTC})_2$ . The phenomenon can in fact be explained considering that upon water removal at low temperature, the solvated Cu(II) ions undergo a local symmetry change, which is ultimately responsible for the loss in the EPR signal. Rehydration of the system will restore the original solvation shell, thus explaining the recovery of the EPR signal and the easy reversibility of the process.

Following the procedure adopted for all of the experiments, we contacted the hydrated sample with increasing doses of ammonia at ambient temperature. This led to a progressive change of the CW EPR spectrum, up to the formation of a new, intense signal, characterized by an asymmetric line shape resonating at  $g \approx 2.12$  whose intensity is about 2 orders of magnitude more intense with respect to the signal of the hydrated sample (Figure 6A). Figure 7 shows the evolution of the CW EPR spectrum as a function of ammonia dosage. The

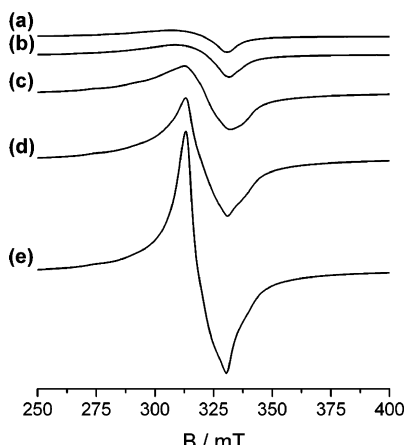


**Figure 7.** X-band CW EPR spectra of HKUST-1 upon delivery of increasing amounts of ammonia. (a) Hydrated sample, (b) 5 mbar of  $\text{NH}_3$ , (c) 30 mbar of  $\text{NH}_3$ , (d) 45 mbar of  $\text{NH}_3$ , and (e) 60 mbar of  $\text{NH}_3$ . Spectra are recorded at 77 K.

new signal starts to appear upon delivery of 30 mbar of  $\text{NH}_3$  and shows no trace of the EPR features of isolated Cu(II), and no echo signals could be detected. Comparison of spectra taken in the range 300–6 K for an ammonia dosage of 30 mbar (Figure 8) shows that no significant modification in the spectral

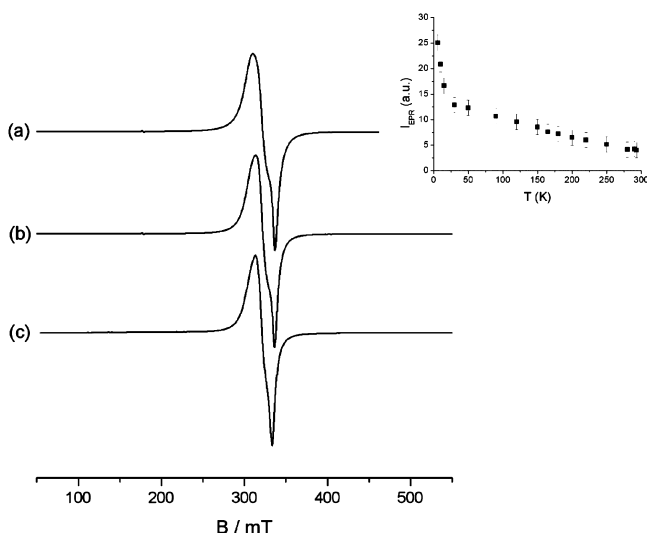


**Figure 8.** CW EPR spectra of HKUST-1 upon delivery of 30 mbar of  $\text{NH}_3$  recorded at (a) 6 K, (b) 90 K, and (c) 300 K. The scattered plot in the inset reports the EPR intensity of the spectra recorded at temperatures ranging from 6 to 300 K.

line shape occurs in this temperature range. The signal intensity, however, increases with lowering temperature following a Curie-like behavior (see inset of Figure 8), typical of a paramagnetic state. The loss of Cu(II) hyperfine structure seems to indicate that spin exchange phenomena are under operation, which involve a large fraction of the copper ions including framework ions. These phenomena will lead to an increase in the relaxation times of the system, explaining the absence of the spin echo signal. The same behavior described above, at least qualitatively, was observed in the case of  $\text{NH}_3$  dosage in dry conditions.

Outgassing of the cell did not restore the original EPR spectrum, indicating that the effect, contrary to water

adsorption, is not reversible and that interaction with  $\text{NH}_3$  leads to a stable modification of the magnetic properties of the sample. Further investigations will be needed to specifically address the nature of the magnetic properties brought about by ammonia adsorption.

#### 4. CONCLUSIONS

A full spectroscopic characterization of HKUST-1 interacting with ammonia has been presented.  $\text{NH}_3$  adsorption on the dry system results in a strong chemisorption on Cu(II) sites that distorts the framework, keeping the crystallinity of the material. Generally, the perturbation observed upon  $\text{NH}_3$  adsorption is analogous to the one observed in the case of  $\text{H}_2\text{O}$ , but noticeably enhanced. When the adsorption in humid conditions is considered, a deep modification of the system is observed. In particular, (i) XRPD shows a very strong interaction in dry conditions and strong modification of the structure in presence of water; (ii) XAS (XANES and EXAFS) spectroscopy, in dry conditions, indicates structural changes, similar to the case of  $\text{H}_2\text{O}$  but quantitatively bigger; (iii) both DRUV-visible and IR (MIR and far-IR frequencies range) spectroscopies indicate a similarity between the hydrated sample and the one interacting with  $\text{NH}_3$  in dry conditions, but they reveal deep changes if  $\text{NH}_3$  is adsorbed in humid conditions; and (iv) EPR technique reveals that the interaction with  $\text{NH}_3$  in both dry and humid conditions leads to a stable modification of the magnetic properties of the sample.

On a methodological ground, it is worth noticing that we used the optimization of XANES spectra to validate the bond distance obtained by EXAFS.

This work demonstrates that to have a very deep structural modification of HKUST-1 when  $\text{NH}_3$  interaction is considered (as, e.g., reported in the literature by Peterson et al.<sup>39</sup>), the water presence is necessary; otherwise, the modification occurs but with minor effect.

#### ■ ASSOCIATED CONTENT

##### Supporting Information

Experimental and simulated HYSCORE spectra at  $g_{\parallel}$  position.

This material is available free of charge via the Internet at <http://pubs.acs.org>.

#### ■ AUTHOR INFORMATION

##### Corresponding Author

\*E-mail: francesca.bonino@unito.it.

##### Notes

The authors declare no competing financial interest.

#### ■ ACKNOWLEDGMENTS

We acknowledge Prof. S. Bordiga for fruitful discussion, Dr. G. Agostini for supporting XRPD measurements and related discussion, and finally S. Nikitenko for the important support during the XAS data collection at ESRF beamline BM26A (DUBBLE). This work has been supported by “Progetti di Ricerca di Ateneo-Compagnia di San Paolo-2011-Linea 1A, ORTO11RRT5 project”.

#### ■ REFERENCES

- Cheetham, A. K.; Ferey, G.; Loiseau, T. *Angew. Chem., Int. Ed.* 1999, 38, 3268–3292.
- James, S. L. *Chem. Soc. Rev.* 2003, 32, 276–288.

- (3) Kitagawa, S.; Kitaura, R.; Noro, S. *Angew. Chem., Int. Ed.* **2004**, *43*, 2334–2375.
- (4) Bradshaw, D.; Claridge, J. B.; Cussen, E. J.; Prior, T. J.; Rosseinsky, M. J. *Acc. Chem. Res.* **2005**, *38*, 273–282.
- (5) Ferey, G. *Chem. Soc. Rev.* **2008**, *37*, 191–214.
- (6) Farha, O. K.; Hupp, J. T. *Acc. Chem. Res.* **2010**, *43*, 1166–1175.
- (7) Stock, N.; Biswas, S. *Chem. Rev.* **2012**, *112*, 933–969.
- (8) Meek, S. T.; Greathouse, J. A.; Allendorf, M. D. *Adv. Mater.* **2011**, *23*, 249–267.
- (9) Wu, C. D.; Hu, A.; Zhang, L.; Lin, W. B. *J. Am. Chem. Soc.* **2005**, *127*, 8940–8941.
- (10) Dybtsev, D. N.; Nuzhdin, A. L.; Chun, H.; Bryliakov, K. P.; Talsi, E. P.; Fedin, V. P.; Kim, K. *Angew. Chem., Int. Ed.* **2006**, *45*, 916–920.
- (11) Llabrés i Xamena, F. X.; Abad, A.; Corma, A.; Garcia, H. *J. Catal.* **2007**, *250*, 294–298.
- (12) Horike, S.; Dinca, M.; Tamaki, K.; Long, J. R. *J. Am. Chem. Soc.* **2008**, *130*, 5854–5855.
- (13) Savonnet, M.; Aguado, S.; Ravon, U.; Bazer-Bachi, D.; Lecocq, V.; Bats, N.; Pinel, C.; Farrusseng, D. *Green Chem.* **2009**, *11*, 1729–1732.
- (14) Lee, J.; Farha, O. K.; Roberts, J.; Scheidt, K. A.; Nguyen, S. T.; Hupp, J. T. *Chem. Soc. Rev.* **2009**, *38*, 1450–1459.
- (15) Shultz, A. M.; Farha, O. K.; Hupp, J. T.; Nguyen, S. T. *J. Am. Chem. Soc.* **2009**, *131*, 4204–4205.
- (16) Ma, L.; Abney, C.; Lin, W. *Chem. Soc. Rev.* **2009**, *38*, 1248–1256.
- (17) Corma, A.; Garcia, H.; Llabrés i Xamena, F. X. *Chem. Rev.* **2010**, *110*, 4606–4655.
- (18) Luz, I.; Xamena, F.; Corma, A. *J. Catal.* **2012**, *285*, 285–291.
- (19) Aguado, S.; Canivet, J.; Schuurman, Y.; Farrusseng, D. *J. Catal.* **2011**, *284*, 207–214.
- (20) Eddaoudi, M.; Kim, J.; Rosi, N.; Vodak, D.; Wachter, J.; O'Keeffe, M.; Yaghi, O. M. *Science* **2002**, *295*, 469–472.
- (21) Dinca, M.; Long, J. R. *J. Am. Chem. Soc.* **2005**, *127*, 9376–9377.
- (22) Dinca, M.; Dailly, A.; Liu, Y.; Brown, C. M.; Neumann, D. A.; Long, J. R. *J. Am. Chem. Soc.* **2006**, *128*, 16876–16883.
- (23) Vitillo, J. G.; Regli, L.; Chavan, S.; Ricchiardi, G.; Spoto, G.; Dietzel, P. D. C.; Bordiga, S.; Zecchina, A. *J. Am. Chem. Soc.* **2008**, *130*, 8386–8396.
- (24) Dietzel, P. D. C.; Johnsen, R. E.; Fjellvag, H.; Bordiga, S.; Groppe, E.; Chavan, S.; Blom, R. *Chem. Commun.* **2008**, 5125–5127.
- (25) Murray, L. J.; Dinca, M.; Long, J. R. *Chem. Soc. Rev.* **2009**, *38*, 1294–1314.
- (26) Li, J.-R.; Luppler, R. J.; Zhou, H. C. *Chem. Soc. Rev.* **2009**, *38*, 1477–1504.
- (27) Britt, D.; Furukawa, H.; Wang, B.; Glover, T. G.; Yaghi, O. M. *Proc. Natl. Acad. Sci. U.S.A.* **2009**, *106*, 20637–20640.
- (28) Sato, H.; Matsuda, R.; Sugimoto, K.; Takata, M.; Kitagawa, S. *Nat. Mater.* **2010**, *9*, 661–666.
- (29) Shimomura, S.; Higuchi, M.; Matsuda, R.; Yoneda, K.; Hijikata, Y.; Kubota, Y.; Mita, Y.; Kim, J.; Takata, M.; Kitagawa, S. *Nat. Chem.* **2010**, *2*, 633–637.
- (30) Hamon, L.; Heymans, N.; Llewellyn, P. L.; Guillerm, V.; Ghoufi, A.; Vaesen, S.; Maurin, G.; Serre, C.; De Weireld, G.; Pirngruber, G. D. *Dalton Trans.* **2012**, *41*, 4052–4059.
- (31) Chavan, S.; Vitillo, J. G.; Gianolio, D.; Zavorotynska, O.; Civalleri, B.; Jakobsen, S.; Nilsen, M. H.; Valenzano, L.; Lamberti, C.; Lillerud, K. P.; et al. *Phys. Chem. Chem. Phys.* **2012**, *14*, 1614–1626.
- (32) Chui, S. S. Y.; Lo, S. M. F.; Charnant, J. P. H.; Orpen, A. G.; Williams, I. D. *Science* **1999**, *283*, 1148–1150.
- (33) Wang, Q. M.; Shen, D. M.; Bulow, M.; Lau, M. L.; Deng, S. G.; Fitch, F. R.; Lemcoff, N. O.; Semanscin, J. *Microporous Mesoporous Mater.* **2002**, *55*, 217–230.
- (34) Xiao, B.; Wheatley, P. S.; Zhao, X. B.; Fletcher, A. J.; Fox, S.; Rossi, A. G.; Megson, I. L.; Bordiga, S.; Regli, L.; Thomas, K. M.; et al. *J. Am. Chem. Soc.* **2007**, *129*, 1203–1209.
- (35) Bordiga, S.; Regli, L.; Bonino, F.; Groppe, E.; Lamberti, C.; Xiao, B.; Wheatley, P. S.; Morris, R. E.; Zecchina, A. *Phys. Chem. Chem. Phys.* **2007**, *9*, 2676–2685.
- (36) Prestipino, C.; Regli, L.; Vitillo, J. G.; Bonino, F.; Damin, A.; Lamberti, C.; Zecchina, A.; Solari, P. L.; Kongshaug, K. O.; Bordiga, S. *Chem. Mater.* **2006**, *18*, 1337–1346.
- (37) Zhang, X. X.; Chui, S. S. Y.; Williams, I. D. *J. Appl. Phys.* **2000**, *87*, 6007–6009.
- (38) Schlichte, K.; Kratzke, T.; Kaskel, S. *Microporous Mesoporous Mater.* **2004**, *73*, 81–88.
- (39) Peterson, G. W.; Wagner, G. W.; Balboa, A.; Mahle, J.; Sewell, T.; Karwacki, C. *J. Phys. Chem. C* **2009**, *113*, 13906–13917.
- (40) Petit, C.; Bandosz, T. J. *Dalton Trans.* **2012**, *41*, 4027–4035.
- (41) Petit, C.; Huang, L. L.; Jagiello, J.; Kenvin, J.; Gubbins, K. E.; Bandosz, T. J. *Langmuir* **2011**, *27*, 13043–13051.
- (42) Petit, C.; Mendoza, B.; Bandosz, T. J. *Langmuir* **2010**, *26*, 15302–15309.
- (43) Saha, D. P.; Deng, S. G. *J. Colloid Interface Sci.* **2010**, *348*, 615–620.
- (44) Guo, X. J.; Tak, J. K.; Johnson, R. L. *J. Hazard. Mater.* **2009**, *166*, 372–376.
- (45) Arreola, R.; Valderrama, B.; Morante, M. L.; Horjales, E. *FEBS Lett.* **2003**, *551*, 63–70.
- (46) Britt, D.; Tranchemontagne, D.; Yaghi, O. M. *Proc. Natl. Acad. Sci. U.S.A.* **2008**, *105*, 11623–11627.
- (47) Kusgens, P.; Rose, M.; Senkovska, I.; Frode, H.; Henschel, A.; Siegle, S.; Kaskel, S. *Microporous Mesoporous Mater.* **2009**, *120*, 325–330.
- (48) Nikitenko, S.; Beale, A. M.; van der Eerden, A. M. J.; Jacques, S. D. M.; Leynaud, O.; O'Brien, M. G.; Detollenaere, D.; Kaptein, R.; Weckhuysen, B. M.; Bras, W. *J. Synchrotron Radiat.* **2008**, *15*, 632–640.
- (49) Silversmit, G.; Vekemans, B.; Nikitenko, S.; Bras, W.; Czhech, V.; Zaray, G.; Szaloki, I.; Vincze, L. *J. Synchrotron Radiat.* **2009**, *16*, 237–246.
- (50) Lamberti, C.; Prestipino, C.; Bordiga, S.; Berlier, G.; Spoto, G.; Zecchina, A.; Laloni, A.; La Manna, F.; D'Anca, F.; Felici, R.; et al. *Nucl. Instrum. Methods Phys. Res., Sect. B* **2003**, *200*, 196–201.
- (51) Lamberti, C.; Bordiga, S.; Bonino, F.; Prestipino, C.; Berlier, G.; Capello, L.; D'Acquisto, F.; Xamena, F.; Zecchina, A. *Phys. Chem. Chem. Phys.* **2003**, *5*, 4502–4509.
- (52) Ravel, B.; Newville, M. *J. Synchrotron Radiat.* **2005**, *12*, 537–541.
- (53) Lamberti, C.; Bordiga, S.; Arduino, D.; Zecchina, A.; Geobaldo, F.; Spanò, G.; Genoni, F.; Petrini, G.; Carati, A.; Villain, F.; et al. *J. Phys. Chem. B* **1998**, *102*, 6382–6390.
- (54) Bordiga, S.; Bonino, F.; Lillerud, K. P.; Lamberti, C. *Chem. Soc. Rev.* **2010**, *39*, 4885–4927.
- (55) Zabinsky, S. I.; Rehr, J. J.; Ankudinov, A.; Albers, R. C.; Eller, M. *J. Phys. Rev. B* **1995**, *52*, 2995–3009.
- (56) Ankudinov, A. L.; Rehr, J. J. *Phys. Rev. B* **2000**, *62*, 2437–2445.
- (57) Smolentsev, G.; Soldatov, A. *J. Synchrotron Radiat.* **2006**, *13*, 19–29.
- (58) Spalek, T.; Pietrzyk, P.; Sojka, Z. *J. Chem. Inf. Model.* **2005**, *45*, 18–29.
- (59) Hofer, P.; Grupp, A.; Nebenfuhr, H.; Mehring, M. *Chem. Phys. Lett.* **1986**, *132*, 279–282.
- (60) Stoll, S.; Schweiger, A. *J. Magn. Reson.* **2006**, *178*, 42–55.
- (61) Lamberti, C.; Spoto, G.; Scarano, D.; Paze, C.; Salvalaggio, M.; Bordiga, S.; Zecchina, A.; Palomino, G. T.; Dacapito, F. *Chem. Phys. Lett.* **1997**, *269*, 500–508.
- (62) Lamberti, C.; Bordiga, S.; Zecchina, A.; Salvalaggio, M.; Geobaldo, F.; Arean, C. O. *J. Chem. Soc., Faraday Trans.* **1998**, *94*, 1519–1525.
- (63) Bolis, V.; Maggiorini, S.; Meda, L.; D'Acquisto, F.; Palomino, G. T.; Bordiga, S.; Lamberti, C. *J. Chem. Phys.* **2000**, *113*, 9248–9261.
- (64) Turnes Palomino, G.; Fisicaro, P.; Bordiga, S.; Zecchina, A.; Giannello, E.; Lamberti, C. *J. Phys. Chem. B* **2000**, *104*, 4064–4073.

- (65) Lamberti, C.; Prestipino, C.; Bonino, F.; Capello, L.; Bordiga, S.; Spoto, G.; Zecchina, A.; Moreno, S. D.; Cremaschi, B.; Garilli, M.; et al. *Angew. Chem., Int. Ed.* **2002**, *41*, 2341–2344.
- (66) Prestipino, C.; Berlier, G.; Xamena, F.; Spoto, G.; Bordiga, S.; Zecchina, A.; Palomino, G. T.; Yamamoto, T.; Lamberti, C. *Chem. Phys. Lett.* **2002**, *363*, 389–396.
- (67) Prestipino, C.; Bordiga, S.; Lamberti, C.; Vidotto, S.; Garilli, M.; Cremaschi, B.; Marsella, A.; Leofanti, G.; Fisicaro, P.; Spoto, G.; et al. *J. Phys. Chem. B* **2003**, *107*, 5022–5030.
- (68) Llabrés i Xamena, F. X.; Fisicaro, P.; Berlier, G.; Zecchina, A.; Palomino, G. T.; Prestipino, C.; Bordiga, S.; Giamello, E.; Lamberti, C. *J. Phys. Chem. B* **2003**, *107*, 7036–7044.
- (69) Prestipino, C.; Capello, L.; D’Acapito, F.; Lamberti, C. *Phys. Chem. Chem. Phys.* **2005**, *7*, 1743–1746.
- (70) Truccato, M.; Lamberti, C.; Prestipino, C.; Agostino, A. *Appl. Phys. Lett.* **2005**, *86*, 213116.
- (71) Muddada, N. B.; Olsbye, U.; Caccialupi, L.; Cavani, F.; Leofanti, G.; Gianolio, D.; Bordiga, S.; Lamberti, C. *Phys. Chem. Chem. Phys.* **2010**, *12*, 5605–5618.
- (72) Muddada, N. B.; Olsbye, U.; Leofanti, G.; Gianolio, D.; Bonino, F.; Bordiga, S.; Fuglerud, T.; Vidotto, S.; Marsella, A.; Lamberti, C. *Dalton Trans.* **2010**, *39*, 8437–8449.
- (73) Groppo, E.; Prestipino, C.; Lamberti, C.; Luches, P.; Giovanardi, C.; Boscherini, F. *J. Phys. Chem. B* **2003**, *107*, 4597–4606.
- (74) Lamberti, C.; Groppo, E.; Prestipino, C.; Casassa, S.; Ferrari, A. M.; Pisani, C.; Giovanardi, C.; Luches, P.; Valeri, S.; Boscherini, F. *Phys. Rev. Lett.* **2003**, *91*, 046101.
- (75) Groppo, E.; Prestipino, C.; Lamberti, C.; Carboni, R.; Boscherini, F.; Luches, P.; Valeri, S.; D’Addato, S. *Phys. Rev. B* **2004**, *70*, 165408.
- (76) Lamberti, C. *Surf. Sci. Rep.* **2004**, *53*, 1–197.
- (77) Piovano, A.; Agostini, G.; Frenkel, A. I.; Bertier, T.; Prestipino, C.; Ceretti, M.; Paulus, W.; Lamberti, C. *J. Phys. Chem. C* **2011**, *115*, 1311–1322.
- (78) Cavka, J. H.; Jakobsen, S.; Olsbye, U.; Guillou, N.; Lamberti, C.; Bordiga, S.; Lillerud, K. P. *J. Am. Chem. Soc.* **2008**, *130*, 13850–13851.
- (79) Bonino, F.; Chavan, S.; Vitillo, J. G.; Groppo, E.; Agostini, G.; Lamberti, C.; Dietzel, P. D. C.; Prestipino, C.; Bordiga, S. *Chem. Mater.* **2008**, *20*, 4957–4968.
- (80) Chavan, S.; Bonino, F.; Vitillo, J. G.; Groppo, E.; Lamberti, C.; Dietzel, P. D. C.; Zecchina, A.; Bordiga, S. *Phys. Chem. Chem. Phys.* **2009**, *11*, 9811–9822.
- (81) Masciocchi, N.; Galli, S.; Colombo, V.; Maspero, A.; Palmisano, G.; Seyyedi, B.; Lamberti, C.; Bordiga, S. *J. Am. Chem. Soc.* **2010**, *132*, 7902–7904.
- (82) Valenzano, L.; Civalleri, B.; Bordiga, S.; Nilsen, M. H.; Jakobsen, S.; Lillerud, K.-P.; Lamberti, C. *Chem. Mater.* **2011**, *23*, 1700–1718.
- (83) Valenzano, L.; Vitillo, J. G.; Chavan, S.; Civalleri, B.; Bonino, F.; Bordiga, S.; Lamberti, C. *Catal. Today* **2012**, *182*, 67–79.
- (84) Rossin, A.; Di Credico, B.; Giambastiani, G.; Peruzzini, M.; Pescitelli, G.; Reginato, G.; Borfecchia, E.; Gianolio, D.; Lamberti, C.; Bordiga, S. *J. Mater. Chem.* **2012**, *22*, 10335–10344.
- (85) Boscherini, F.; Lamberti, C.; Pasarelli, S.; Rigo, C.; Mobilio, S. *Phys. Rev. B* **1998**, *58*, 10745–10753.
- (86) Romanato, F.; De Salvador, D.; Berti, M.; Drigo, A.; Natali, M.; Tormen, M.; Rossetto, G.; Pasarelli, S.; Boscherini, F.; Lamberti, C.; et al. *Phys. Rev. B* **1998**, *57*, 14619–14622.
- (87) Pöppl, A.; Kunz, S.; Himsel, D.; Hartmann, M. *J. Phys. Chem. C* **2008**, *112*, 2678–2684.
- (88) Jee, B.; Eisinger, K.; Gul-E-Noor, F.; Bertmer, M.; Hartmann, M.; Himsel, D.; Pöppl, A. *J. Phys. Chem. C* **2010**, *114*, 16630–16639.
- (89) Jee, B.; Koch, K.; Moschkowitz, L.; Himsel, D.; Hartman, M.; Pöppl, A. *J. Phys. Chem. Lett.* **2011**, *2*, 357–361.
- (90) Gul-E-Noor, F.; Jee, B.; Pöppl, A.; Hartmann, M.; Himsel, D.; Bertmer, M. *Phys. Chem. Chem. Phys.* **2011**, *13*, 7783–7788.
- (91) Pöppl, A.; Kevan, L. *J. Phys. Chem.* **1996**, *100*, 3387–3394.
- (92) Atherton, N. M.; Horsewill, A. *J. Mol. Phys.* **1979**, *37*, 1349–1361.
- (93) Jang, H. J.; Hall, W. K.; d’Itri, J. L. *J. Phys. Chem.* **1996**, *100*, 9416–9420.
- (94) Larsen, S. C.; Aylor, A.; Bell, A. T.; Reimer, J. A. *J. Phys. Chem.* **1994**, *98*, 11533–11540.
- (95) Lo Jacono, M.; Fierro, G.; Dragone, R.; Feng, X. B.; d’Itri, J.; Hall, W. K. *J. Phys. Chem. B* **1997**, *101*, 1979–1984.